

Thermoelectric transport in surface- and antimony-doped bismuth telluride nanoplates

Michael Thompson Pettes,^{1,2} Jaehyun Kim,¹ Wei Wu,² Karen C. Bustillo,³ and Li Shi^{1,a}

¹*Department of Mechanical Engineering, The University of Texas at Austin, Austin, Texas 78712, USA*

²*Department of Mechanical Engineering and Institute of Materials Science, University of Connecticut, Storrs, Connecticut 06269, USA*

³*National Center for Electron Microscopy, Molecular Foundry, Lawrence Berkeley National Laboratory, Berkeley, California 94720, USA*

(Received 21 March 2016; accepted 24 June 2016; published online 25 July 2016)

We report the in-plane thermoelectric properties of suspended $(\text{Bi}_{1-x}\text{Sb}_x)_2\text{Te}_3$ nanoplates with x ranging from 0.07 to 0.95 and thicknesses ranging from 9 to 42 nm. The results presented here reveal a trend of increasing *p*-type behavior with increasing antimony concentration, and a maximum Seebeck coefficient and thermoelectric figure of merit at $x \sim 0.5$. We additionally tuned extrinsic doping of the surface using a tetrafluoro-tetracyanoquinodimethane ($\text{F}_4\text{-TCNQ}$) coating. The lattice thermal conductivity is found to be below that for undoped ultrathin Bi_2Te_3 nanoplates of comparable thickness and in the range of $0.2\text{--}0.7 \text{ W m}^{-1} \text{ K}^{-1}$ at room temperature. © 2016 Author(s). All article content, except where otherwise noted, is licensed under a Creative Commons Attribution (CC BY) license (<http://creativecommons.org/licenses/by/4.0/>). [<http://dx.doi.org/10.1063/1.4955400>]

Bismuth telluride (Bi_2Te_3) is one of the most commonly used thermoelectric materials.^{1,2} It was predicted over two decades ago that quantum confinement of electrons in two-dimensional Bi_2Te_3 layers can result in enhanced thermoelectric power factor $S^2\sigma$, where S is the Seebeck coefficient and σ is the electrical conductivity.³ Recent experimental observations of surface electronic states protected by time-reversal symmetry in bismuth chalcogenides, including Bi_2Te_3 ,⁴ Bi_2Se_3 ,⁵ and BiSbTeSe_2 ,⁶ have also led to theoretical predictions of enhancement of the thermoelectric performance in ultrathin layers of these so-called topological insulators.^{7,8} The enhancement is predicted in ultrathin bismuth chalcogenides with a precise control of the Fermi level and carrier concentration. However, bismuth chalcogenides synthesized by different methods often suffer from chalcogen vacancies in the bulk crystal^{9,10} and surface doping from exposure to the air environment,^{11,12} both of which make these materials degenerate *n*-type semiconductors with reduced thermoelectric power factors. In ultrathin materials, the extrinsic *n*-type environmental surface doping can dominate the intrinsic *p*-type surface dipole arising from topological surface state occupation.¹³

Several methods to modulate the carrier concentration and optimize the Fermi energy in these ultrathin samples have been reported. These methods involve substitutional doping of Ca¹⁴ and Sb^{15,16} on the Bi atomic sites in order to optimize the Fermi energy and maximize the contribution from the protected surface states. Two especially relevant advances to tune the Fermi energy in Bi_2Te_3 involve doping with antimony^{15,16} to create $(\text{Bi}_{1-x}\text{Sb}_x)_2\text{Te}_3$ in the range between $x = 0$ (Bi_2Te_3) and $x = 1$ (Sb_2Te_3). Trends in both studies are similar: antimony incorporation lowers the Fermi energy, although the studies differ on the exact composition that leads to the so-called bulk-insulating electron transport, $x = 0.50$, in one work¹⁵ and $x = 0.96$ in the other.¹⁶ It is noted that these x values were defined by the source material composition. This trend has the effect of changing the majority carrier type from electrons in Bi-rich samples to holes in

^aAuthor to whom correspondence should be addressed. Electronic mail: lishi@mail.utexas.edu.

Sb-rich samples, which has been confirmed by Hall measurements.¹⁵ Additionally, to offset the effect of extrinsic environmental doping, highly electronegative hole-injecting molecules, such as NO_2 ¹⁴ and tetrafluoro-tetracyanoquinodimethane ($\text{F}_4\text{-TCNQ}$),¹⁷ have been employed to control the surface potential of two-dimensional (2D) graphene,^{18,19} ultrathin Bi_2Se_3 ,¹⁷ and WSe_2 ²⁰ but not yet for Bi_2Te_3 . Although there are several compatible molecules for use as surface dopants,²¹ $\text{F}_4\text{-TCNQ}$ has often been used for proof-of-concept investigations as it provides a very strong surface *p*-type doping effect compared to other hole injecting molecules due to its high electron affinity of ~ 5.2 eV. This surface-effect has been experimentally observed in $\text{F}_4\text{-TCNQ}$ -coated graphene by angle-resolved photoemission spectroscopy (ARPES).¹⁹ Although these compositional and surface doping methods appear to be promising, their effects on thermoelectric transport in ultrathin topological insulator materials such as Bi_2Te_3 remain elusive.

Here we report measurements of the three in-plane transport properties—thermal conductivity (κ), electrical conductivity ($\sigma \equiv \rho^{-1}$, where ρ is the electrical resistivity), and Seebeck coefficient (S)—that enter the expression for thermoelectric figure of merit, $zT = (S^2\sigma/\kappa)T$, on thin $(\text{Bi}_{1-x}\text{Sb}_x)_2\text{Te}_3$ nanoplates with x ranging from 0.07 to 0.95. The carrier concentration in the nanoplates is varied by antimony substitution, while the surface potential is tuned by direct deposition of a hole-injecting molecule, $\text{F}_4\text{-TCNQ}$, onto all surfaces of individually measured suspended nanoplates. We observe a maximum *p*-type Seebeck coefficient and corresponding maximum zT at $x = 0.5$ and a general *p*-type doping effect upon exposure to $\text{F}_4\text{-TCNQ}$. This surface effect is efficient enough to allow observation of a remarkable change of the majority carrier type from electrons to holes in a lightly doped ($x = 0.07$), 9 nm-thick sample.

We have used a chemical vapor deposition (CVD) method to synthesize the $(\text{Bi}_{1-x}\text{Sb}_x)_2\text{Te}_3$ nanoplates (NPs) on SiO_2 -coated Si substrates similar to that demonstrated in previous reports.^{12,15,22} Incorporation of Sb is achieved by varying the molar ratio of Bi_2Te_3 and Sb_2Te_3 source materials.¹⁵ The mole fractions of Sb dopants reported here as x in $(\text{Bi}_{1-x}\text{Sb}_x)_2\text{Te}_3$ correspond to that in the precursors. Random incorporation of Sb on Bi atomic sites is facilitated by the comparable lattice parameters and crystal symmetry of these materials (Figure 1(a)) as has been verified in detail by a previous work.¹⁵ We have measured the composition of three samples ($x = 0.07$, 0.25, and 0.50) using two different electron microscopes with two different high sensitivity energy dispersive x-ray spectroscopy (EDS) detectors (FEI Nova NanoSEM 450 with an Oxford X-Max 80 XMX1105 silicon drift detector; FEI 80-300 TitanX with a FEI Super-X Quad windowless silicon drift detector system). Variation between instruments is large, with up to 2933% variation in the calculated Sb content and a 595% variation in the value of Te deficiency. A large variation is observed even for the same instrument, which can be attributed to two mechanisms: (1) the irradiated sample volume is very small due to the very thin samples, and (2) even for large sample volumes, EDS is seen as a qualitative tool where uncertainty can be on the order of several percent.²³ For this reason we have chosen to list Sb content x in our samples as the nominal molar ratio of Bi:Sb in the source materials as well as to allow fair comparison with previous reports, which have also reported x using the molar ratio of source precursors.^{15,16} We note that accurate determination of molecular composition is a critical challenge and while techniques

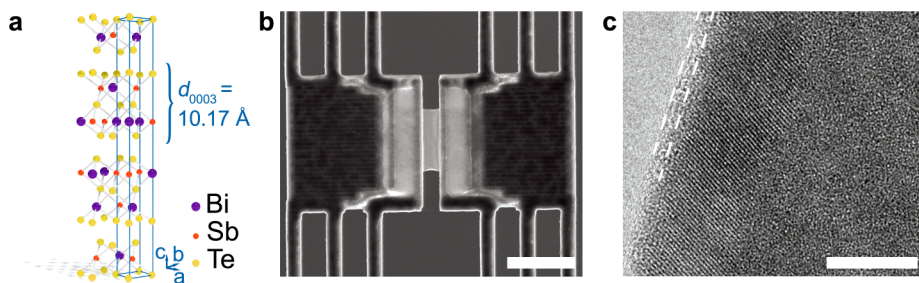


FIG. 1. (a) Crystal structure of the 2D layered material $(\text{Bi}_{1-x}\text{Sb}_x)_2\text{Te}_3$, where each quintuple layer is 10.17 Å thick.³² (b) Scanning electron and (c) transmission electron micrographs of the sample with $x = 0.5$ transferred onto a micro-bridge device, taken after deposition and removal of excess organic molecule $\text{F}_4\text{-TCNQ}$. The boundaries of the nanoplate and amorphous coating are depicted by dashed lines. Scale bars are 10 μm for (b) and 10 nm for (c).

such as inductively coupled plasma mass spectrometry (ICP-MS) offer better than part per billion accuracy, the technique is designed for large volume samples with more than several mg in mass.²⁴

After growth, the samples were transferred to a suspended micro-thermometry test platform (Figure 1(b)) using an electrochemically sharpened probe. Transfer was performed in ambient conditions under an optical microscope. Samples were then placed into a variable-temperature cryostat, within roughly 2–10 h after growth. The electrical, thermal, and thermoelectric properties of the nanoplates have been obtained with the same four-probe thermoelectric measurement method as reported previously.^{12,25} The sample was first held at the maximum temperature (~450 K) for several hours, after which the sample stage temperature was gradually lowered to each measurement temperature. Electrical contact to the nanoplate sample was obtained by electrical current annealing at ~450 K. Transmission electron microscopy (TEM) analysis was performed after transport measurements were conducted (Figure 1(c)).

Additionally, we have characterized the compositional stability of the $x = 0.5$ and $x = 0.07$ samples after storage in an inert atmosphere for two years (Figure 2). EDS was used to qualitatively map the compositional homogeneity of the nanoplates in an uncorrected FEI Titan 80-300 TEM operating at 120 kV using a FEI Super-X Quad windowless detector based on silicon drift technology with a solid angle of 0.7 sr. We found a uniform distribution of Sb atoms within the structures in the $x = 0.5$ sample, as opposed to segregated Bi_2Te_3 and Sb_2Te_3 phases.

The measured thermoelectric properties are shown in Figures 3–5. The thicknesses, geometry, and room-temperature properties for the five $(\text{Bi}_{1-x}\text{Sb}_x)_2\text{Te}_3$ samples in this work are listed in Table I, where the Sb content, $x = 0.07, 0.25, 0.5, 0.7$, and 0.95 , are nominally based on the precursor composition.

It has been suggested by a recent study that the measured Bi_2Te_3 nanoplates synthesized by a similar method were unintentionally doped.¹² Additionally, it was suggested that exposure to air resulted in *n*-type surface band-bending on the order of 230 meV,¹² which is in qualitative agreement with that observed by ARPES.¹¹ In contrast to the degenerate behavior observed in the Bi_2Te_3 samples measured in the previous work¹² and the current $(\text{Bi}_{1-x}\text{Sb}_x)_2\text{Te}_3$ samples with $x = 0.5$ and higher, where the measured electrical conductivity decreases with increasing temperature, opposite temperature dependence expected for non-degenerate semiconductors was observed in the two samples with $x = 0.07$ and 0.25 (Figure 3(a)). In comparison, a similar non-degenerate or so-called bulk insulating behavior was observed at high Sb-doping levels in the x range of 0.75–0.98 (determined by MBE precursor flux composition) in another experiment with $(\text{Bi}_{1-x}\text{Sb}_x)_2\text{Te}_3$ thin layers,¹⁶ likely due to differences in sample thickness, synthesis conditions, and chemical compositions in the samples synthesized from source materials with similar x .

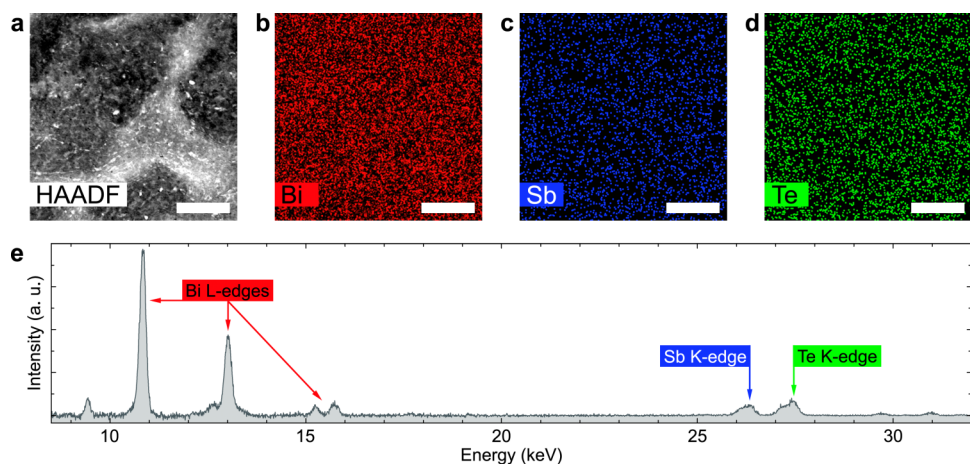


FIG. 2. Energy dispersive x-ray spectroscopy (EDS) analysis of aged $(\text{Bi}_{1-x}\text{Sb}_x)_2\text{Te}_3$ nanoplates for $x = 0.50$ shows uniform antimony distribution across the nanoplate after two years of storage in an inert atmosphere, scale bar is 500 nm. (a) High-angle annular dark-field image, contrast is from carbon thickness; (b) Bi L-edge; (c) Sb K-edge; (d) Te K-edge. (e) Background-corrected spectrum shows the signal to noise ratio of respective edges.

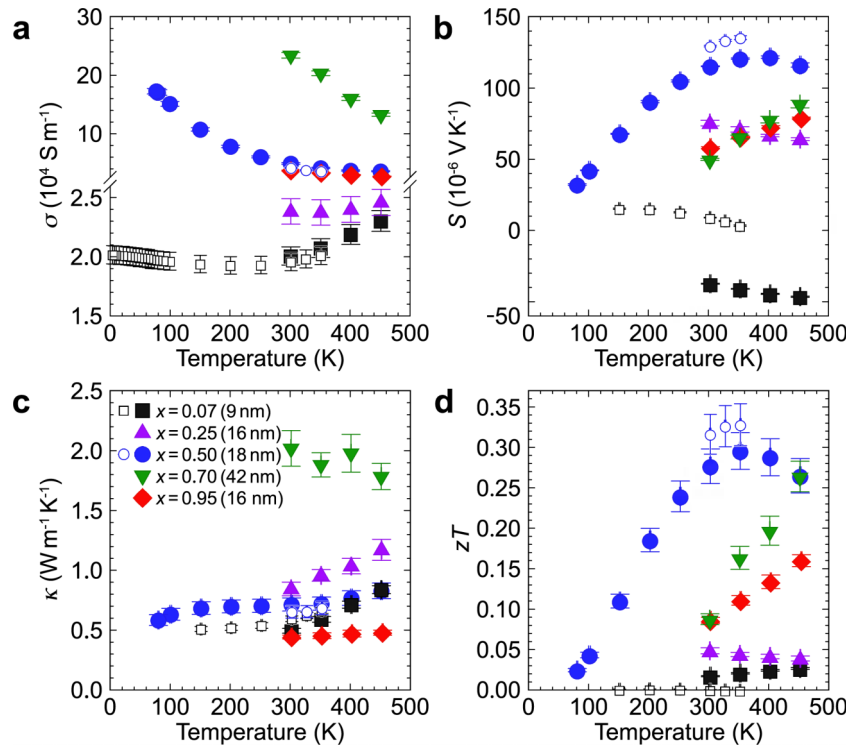


FIG. 3. Measured temperature-dependent thermoelectric properties of individual $(\text{Bi}_{1-x}\text{Sb}_x)_2\text{Te}_3$ nanoplates. (a) Electrical conductivity, σ , (b) Seebeck coefficient, S , (c) thermal conductivity, κ , and (d) thermoelectric figure of merit, $zT = (S^2\sigma/\kappa)T$, as a function of temperature. Results for as-grown samples (filled symbols) and after deposition and removal of excess organic molecule F4-TCNQ (open symbols) indicate the *p*-type surface doping effect of the molecule. The legend shown in (c) applies to panels ((a)–(d)), nanoplate thicknesses are listed in parentheses.

The Seebeck coefficient of the $(\text{Bi}_{1-x}\text{Sb}_x)_2\text{Te}_3$ NPs exhibits a clear dependence on the amount of Sb substitution (Figures 3(b) and 4(b)). At a low Sb substitution level of $x = 0.07$, the Seebeck coefficient is negative and the lowest in magnitude of all samples. The low Seebeck coefficient and non-degenerate electrical conductivity of this sample suggests that it is in the intrinsic regime. Sb-doping at x near 0.25 and higher resulted in positive Seebeck coefficients at near room temperature, with a maximum of $115 \mu\text{V K}^{-1}$ at $x = 0.5$. As with Bi_2Te_3 nanoplates, the magnitude of S for the Sb-substituted nanoplates was reduced considerably compared to the maximum reported bulk Bi_2Te_3 values, 225 and $-250 \mu\text{V K}^{-1}$ for *p*- and *n*-type, respectively, at room temperature.^{26,27} The positive and negative Seebeck coefficient values suggest that the majority carriers are holes and electrons, respectively. It is noted that the measurement device used here is not able to obtain Hall coefficient data on the same suspended sample for which the thermoelectric properties are measured. In principle, the sign of the Hall coefficient and the Seebeck coefficient can disagree for a mixed carrier sample with high minority-to-majority carrier mobility ratio, for example in multi-band conductors such as single crystalline LaAgSb_2 .²⁸ For Bi_2Te_3 the electron and hole mobilities are similar.^{26,27} Therefore, we do not expect the sign of the Seebeck coefficient in this system to differ from that expected for its Hall coefficient. We note that obtaining the dominant carrier type from Seebeck coefficient measurements is an established practice for Bi_2Te_3 and the $(\text{Bi}_{1-x}\text{Sb}_x)_2\text{Te}_3$ system.^{2,27,29–31} While the measured Seebeck coefficient suggests *p*-type transport for the samples with $x = 0.25$ or higher, *p*-type transport was observed only for $x \geq 0.94$ in an earlier work,¹⁶ where x is defined by the precursor flux composition in molecular beam epitaxy (MBE). In contrast, *p*-type behavior was only observed for samples with $x < 0.5$ in another work,¹⁵ where x is defined by the source composition. These different results in the majority carrier type trend reflect large variations in the actual composition or extrinsic surface doping in these thin nanoplates synthesized in different setups.

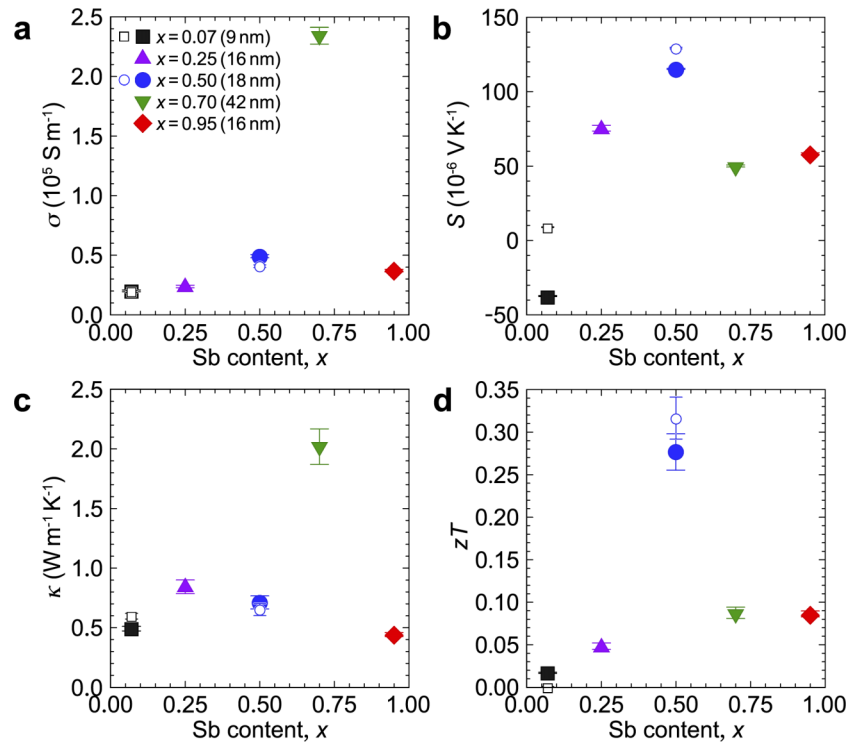


FIG. 4. Measured room temperature concentration-dependent thermoelectric properties of $(\text{Bi}_{1-x}\text{Sb}_x)_2\text{Te}_3$ nanoplates. (a) Electrical conductivity, σ , (b) Seebeck coefficient, S , (c) thermal conductivity, κ , and (d) thermoelectric figure of merit, $zT = (S^2\sigma/\kappa)T$, as a function of antimony concentration, x , for as-grown samples (filled symbols) and after deposition and removal of excess F4-TCNQ (open symbols). The legend shown in (a) applies to panels ((a)-(d)), nanoplate thicknesses are listed in parentheses.

In samples with thicknesses below 18 nm ($x = 0.07, 0.25, 0.5, 0.95$), the total thermal conductivity of the ultrathin $(\text{Bi}_{1-x}\text{Sb}_x)_2\text{Te}_3$ NPs is lower than that reported previously for ultrathin undoped Bi_2Te_3 with comparable thicknesses.¹² The room-temperature total κ for these samples is on the order of $0.4\text{--}0.8 \text{ W m}^{-1} \text{ K}^{-1}$ (Figures 3(c) and 4(c)) and is well below the basal-plane values reported for bulk *n*- and *p*-type Bi_2Te_3 ,²⁷ although differences in sample thickness and electronic contribution to κ make extraction of the alloy scattering effects on the lattice thermal conductivity non-trivial. For the sample with $x = 0.7$, which is $\sim 42 \text{ nm}$ thick, κ is roughly double that of the other samples and decreases with increasing temperature. We also note that these values for total κ are also below the lattice thermal conductivity of similarly doped bulk $(\text{Bi}_{1-x}\text{Sb}_x)_2\text{Te}_3$.²

Despite the reduced lattice thermal conductivity, the reduced Seebeck coefficient has limited zT in the NPs (Figures 3(d) and 4(d)). The zT value reached a maximum in the as-grown samples of 0.30 for $x = 0.5$ at $\sim 350 \text{ K}$. This value is an improvement over the maximum zT of 0.24 measured for undoped, $\sim 9\text{--}25 \text{ nm}$ -thick Bi_2Te_3 NPs in a previous work.¹²

Since the charge carrier concentration affects both σ and κ , we compare the properties of the $(\text{Bi}_{1-x}\text{Sb}_x)_2\text{Te}_3$ NPs with those of un-intentionally doped Bi_2Te_3 NPs¹² and bulk Bi_2Te_3 ²⁷ by plotting κ versus σ (Figure 5(a)) and S versus σ (Figure 5(b)). We observe a general trend of decreasing κ with decreasing σ for the measured samples (Figure 5(a)), with both lower values of σ and κ achieved than for undoped Bi_2Te_3 for all samples except $x = 0.7$, which exhibits high electrical conductivity but still exhibits lower κ than both Bi_2Te_3 NPs and bulk Bi_2Te_3 at similar σ . We also observe an unusual trend of increasing S with σ (Figure 5(b)) for all samples except for $x = 0.7$, which exhibits a relatively low S and high σ . The transport properties in these nanoplates are a function of thickness, therefore the observation that the $x = 0.7$ sample does not follow compositional trends shown in Figure 5(b) likely arises from its thickness of $\sim 42 \text{ nm}$, more than twice that of the other samples, which is expected to result in reduced diffuse surface-electron and surface-phonon scattering rates.¹²

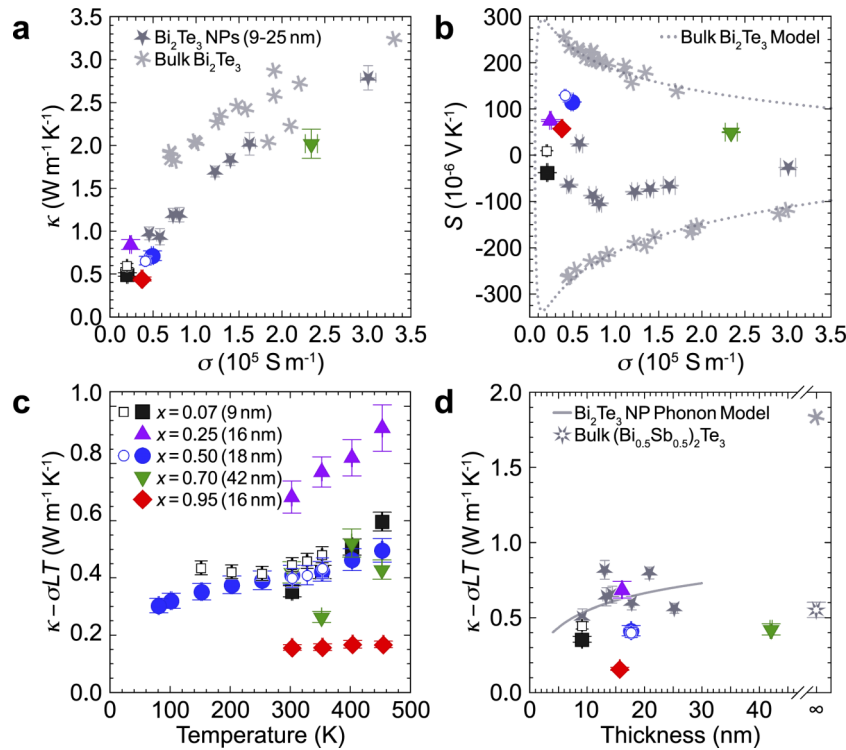


FIG. 5. (a) Measured total thermal conductivity, κ , plotted versus electrical conductivity, σ , for $(\text{Bi}_{1-x}\text{Sb}_x)_2\text{Te}_3$ nanoplates (NPs) shown in comparison with values reported for bulk Bi_2Te_3 in the basal plane²⁷ (asterisks) and values for undoped Bi_2Te_3 NPs¹² (stars). (b) Measured Seebeck coefficient, S , versus σ for the $(\text{Bi}_{1-x}\text{Sb}_x)_2\text{Te}_3$ nanoplates (NPs) shown in comparison with values reported for bulk Bi_2Te_3 in the basal plane²⁶ (asterisks), values for undoped Bi_2Te_3 NPs¹² (stars), and the theoretical value for bulk Bi_2Te_3 in the basal plane¹² (dotted line). (c) Temperature- and (d) thickness-dependent lattice contribution to the thermal conductivity for the $(\text{Bi}_{1-x}\text{Sb}_x)_2\text{Te}_3$ NPs calculated by the Wiedemann-Franz law, $\kappa - \sigma LT$, where the Lorenz number, L , has been obtained from a previously reported model¹² and the measured thermoelectric properties. The $\kappa - \sigma LT$ for undoped Bi_2Te_3 NPs¹² (stars), κ_{lattice} calculated for Bi_2Te_3 from a phonon transport model in the diffuse boundary scattering regime¹² (line), and κ_{lattice} for bulk Bi_2Te_3 ²⁶ (asterisks) and bulk $(\text{Bi}_{0.5}\text{Sb}_{0.5})_2\text{Te}_3$ ² (unfilled stars) in the basal plane are shown in (d) for comparison. Results for as-grown samples (filled symbols) and after deposition and removal of excess organic molecule F₄-TCNQ (open symbols) indicate the surface doping procedure and remaining organic monolayers did not result in observable damage of the suspended NPs or contribute significantly to the measured total thermal conductance. The value of $\kappa - \sigma LT$ for the sample with $x = 0.5$ (green circle) is nearly identical before and after F₄-TCNQ deposition. The legend shown in (a) applies to panels ((a), (b), and (d)), the legend shown in (c) applies to panels ((a)–(d)), nanoplate thicknesses are listed in parentheses.

To gain further insight into thermal transport mechanisms in the ultrathin $(\text{Bi}_{1-x}\text{Sb}_x)_2\text{Te}_3$ NPs, we determine the lattice contribution to the thermal conductivity using the Wiedemann-Franz law as $\kappa - \sigma LT$ where L is the Lorenz number and T is the absolute temperature. To obtain the Lorenz number, we use our measured thermoelectric properties together with an *ab initio* model reported previously.¹² Although this model reports L for the case of flat electronic bands and neglects band bending, this treatment is more appropriate than estimation based on the metallic limit of L_0 . As shown in Figures 5(c) and 5(d), the room temperature values of $\kappa - \sigma LT$ are on the order of 0.2–0.7 W m⁻¹ K⁻¹ for all samples, and the trend of increasing κ_{lattice} with increasing temperature suggests that surface and defect scattering of phonons dominate for all the samples measured here. The result also implies that the high total κ for $x = 0.7$ is due to its high electrical conductivity likely arising from a higher carrier concentration and possibly a lower electron-boundary scattering rate in the thicker sample. In comparison, undoped Bi_2Te_3 nanoplates with thicknesses from ~9 to 25 nm were found to possess lattice thermal conductivities on the order of 0.5–0.8 W m⁻¹ K⁻¹,¹² which is 1.2–3.1 times higher than the doped samples of this work. The difference can be attributed to additional alloy scattering in the $(\text{Bi}_{1-x}\text{Sb}_x)_2\text{Te}_3$ samples studied here. Additionally, the room temperature κ_{lattice} for bulk compounds

TABLE I. Summary of sample dimensions and room temperature thermoelectric properties for as-grown and F₄-TCNQ-surface doped (Bi_{1-x}Sb_x)₂Te₃ nanoplates. The specified Sb content is nominally based on the composition of precursor materials. The lattice contribution to the thermal conductivity has been calculated as $\kappa - \sigma LT$, where L is obtained from a previous model¹² based on the measured thermoelectric properties.

Sb content	Thickness (nm)	Width (μm)	Suspended length (μm)	$\sigma (10^4 \Omega/\text{m})$		$S (10^{-6} \text{ V/K})$		$\kappa (\text{W}/(\text{m K}))$		$\kappa - \sigma LT (\text{W}/(\text{m K}))$
				As-grown	F ₄ -TCNQ	As-grown	F ₄ -TCNQ	As-grown	F ₄ -TCNQ	As-grown
$x = 0.07$	9.1 ± 0.1	12.11 ± 0.31	1.37 ± 0.02	2.01 ± 0.08	1.96 ± 0.07	-37.4 ± 0.3	8.7 ± 0.2	0.50 ± 0.02	0.60 ± 0.02	0.35 ± 0.02
$x = 0.25$	16.1 ± 0.1	8.57 ± 0.19	3.06 ± 0.10	2.38 ± 0.11	...	75.4 ± 1.9	...	0.84 ± 0.06	...	0.69 ± 0.06
$x = 0.50$	17.7 ± 0.1	9.25 ± 0.04	2.58 ± 0.19	4.92 ± 0.13	4.09 ± 0.11	115.2 ± 0.3	129.2 ± 0.6	0.71 ± 0.06	0.65 ± 0.05	0.41 ± 0.03
$x = 0.70$	42.1 ± 0.2	6.70 ± 0.14	8.00 ± 0.27	23.42 ± 0.70	...	50.0 ± 0.7	...	2.02 ± 0.17	...	0.42 ± 0.04
$x = 0.95$	15.7 ± 0.1	18.80 ± 0.41	12.00 ± 0.41	3.72 ± 0.11	...	58.2 ± 0.6	...	0.44 ± 0.02	...	0.16 ± 0.01

reaches a minimum of $0.6\text{--}0.7 \text{ W m}^{-1} \text{ K}^{-1}$ for $(\text{Bi}_{0.5}\text{Sb}_{0.5})_2\text{Te}_3$,² which is 1.3–1.9 times higher than the nanoplate sample with $x = 0.5$ reported here.

Because extrinsic doping of the $(\text{Bi}_{1-x}\text{Sb}_x)_2\text{Te}_3$ nanoplates arising from exposure to ambient conditions during the transfer process can potentially result in *n*-type band bending similar to previous reports for thin Bi_2Te_3 ,^{11,12} we have performed additional thermoelectric transport measurements on nanoplates with $x = 0.07$ and 0.50 before and after deposition of a highly electronegative organic molecule, $\text{F}_4\text{-TCNQ}$ (open symbols, Figures 3–5). After initial measurements, each sample was loaded into a vacuum furnace with several mg of $\text{F}_4\text{-TCNQ}$, and a thin layer of $\text{F}_4\text{-TCNQ}$ was evaporated onto all surfaces of the suspended sample for 10–20 min at a furnace temperature of 100°C . A thick coating was clearly present on both the sample and device upon inspection under an optical microscope. Each sample was immediately transferred back into the cryostat and measurements were conducted after holding the sample at $350\text{--}375 \text{ K}$ for about 12 h to remove excess $\text{F}_4\text{-TCNQ}$. After these measurements, no excess $\text{F}_4\text{-TCNQ}$ was observed using an optical microscope and an amorphous coating of less than 3 nm was observed in the TEM image (Figure 1(c)), similar to the amorphous oxidation layer observed in these samples without the organic coating. These results suggest that vacuum annealing at $350\text{--}375 \text{ K}$ for 12 h is sufficient to remove the majority of $\text{F}_4\text{-TCNQ}$.

The removal of excess $\text{F}_4\text{-TCNQ}$ is indicated in our post-deposition room-temperature thermal conductance measurements. For the $x = 0.07$ sample as an example, we observed a large conductance increase ($2.7\times$) after depositing a thick layer of the organic molecule. After annealing the sample at 50°C overnight, we observed that the thermal conductance returns to near the value for the as-grown nanoplate indicating sublimation of excess $\text{F}_4\text{-TCNQ}$. For the $x = 0.50$ nanoplate, which was annealed at 75°C overnight after $\text{F}_4\text{-TCNQ}$ deposition, we observed a reduction in thermal conductance by $\sim 9\%$, an increase in electrical resistance by $\sim 20\%$, and an increase in the Seebeck coefficient by $\sim 12\%$ at room temperature. In the $x = 0.07$ nanoplate, the application of $\text{F}_4\text{-TCNQ}$ resulted in remarkable changes of the thermoelectric properties, increasing the electrical resistance by $\sim 5\%$ and switching the sign of the Seebeck coefficient from *n*-type to *p*-type transport. Additionally, this modulation of surface potential in the heavily doped $x = 0.5$ sample allows us to probe the effective Lorenz number in this sample. We attribute the changes in electrical and thermal conductances to a small change in band energies at the surface and have extracted an effective Lorenz number of $L = \Delta\kappa/(\Delta\sigma T) = (2.69 \pm 0.05) \times 10^{-8} \text{ W } \Omega \text{ K}^{-2}$ at 300 K . This value compares favorably with the metallic limit of $L_0 = \pi^2 k_B^2/(3 \times 10^2) = 2.44 \times 10^{-8} \text{ W } \Omega \text{ K}^{-2}$. With the application and removal of excess $\text{F}_4\text{-TCNQ}$, the room temperature zT increased by 18% for the $x = 0.5$ sample compared to the as-grown sample and a maximum zT of 0.33 was observed at $\sim 350 \text{ K}$, an 11% increase over the as-grown sample.

These results indicate that both chemical alloying and surface potential modification can play important roles in optimizing the thermoelectric properties in ultrathin $(\text{Bi}_{1-x}\text{Sb}_x)_2\text{Te}_3$ nanoplates. The thermoelectric transport properties of individual $(\text{Bi}_{1-x}\text{Sb}_x)_2\text{Te}_3$ nanoplates ranging in thickness from 9 to 42 nm and with antimony concentrations ranging from $x = 0.07\text{--}0.95$ have been found to exhibit a maximum Seebeck coefficient and thermoelectric figure of merit for the $x = 0.5$ sample. Antimony substitution is found to alter the majority carrier type from electrons for $x \leq 0.07$ to holes for $x \geq 0.25$. The addition of a highly electronegative organic molecule is found to dope the surface of the nanoplates to become more *p*-type even with a very thin coating of only a few nm and increase the maximum zT further. Additionally, we find that the lattice thermal conductivity is reduced compared to a diffuse surface-phonon scattering model indicating the potentially important role of alloy scattering and defect scattering in the samples.

The work at The University of Texas is supported in parts by the Microsystems Technology Office of the U.S. Defense Advanced Research Projects Agency, Award No. N66001-11-1-4107 (M.T.P. and L.S.), and by the Office of Basic Energy Sciences, U.S. Department of Energy, Award No. DE-FG02-07ER46377 (J.K.). Work by W.W. and M.T.P. at the University of Connecticut is supported by the National Science Foundation under Grant No. CAREER-1553987, the UConn Research Foundation, Award No. PD15-0067, and a FEI Company Graduate Fellowship (W.W.). Transmission electron microscopy performed at the Molecular Foundry by W.W. and K.C.B. was

supported by the Office of Science, Office of Basic Energy Sciences, of the U.S. Department of Energy under Contract No. DE-AC02-05CH11231.

- ¹ G. S. Nolas, J. Sharp, and H. J. Goldsmid, *Thermoelectrics: Basic Principles and New Materials Developments* (Springer-Verlag, Heidelberg, Germany, 2001), <http://www.springer.com/us/book/9783540412458>.
- ² D. M. Rowe, *CRC Handbook of Thermoelectrics: Macro to Nano* (CRC Press/Taylor & Francis, New York, 2006), <https://www.crcpress.com/Thermoelectrics-Handbook-Macro-to-Nano/Rowe/9780849322648>.
- ³ L. D. Hicks and M. S. Dresselhaus, *Phys. Rev. B* **47**, 12727 (1993).
- ⁴ Y. L. Chen, J. G. Analytis, J.-H. Chu, Z. K. Liu, S.-K. Mo, X. L. Qi, H. J. Zhang, D. H. Lu, X. Dai, Z. Fang, S. C. Zhang, I. R. Fisher, Z. Hussain, and Z.-X. Shen, *Science* **325**, 178 (2009).
- ⁵ Y. Xia, D. Qian, D. Hsieh, L. Wray, A. Pal, H. Lin, A. Bansil, D. Grauer, Y. S. Hor, R. J. Cava, and M. Z. Hasan, *Nat. Phys.* **5**, 398 (2009).
- ⁶ Y. Xu, I. Miotkowski, C. Liu, J. Tian, H. Nam, N. Alidoust, J. Hu, C.-K. Shih, M. Z. Hasan, and Y. P. Chen, *Nat. Phys.* **10**, 956 (2014).
- ⁷ P. Ghaemi, R. S. K. Mong, and J. E. Moore, *Phys. Rev. Lett.* **105**, 166603 (2010).
- ⁸ Y. Xu, Z. Gan, and S.-C. Zhang, *Phys. Rev. Lett.* **112**, 226801 (2014).
- ⁹ H. J. Noh, H. Koh, S. J. Oh, J. H. Park, H. D. Kim, J. D. Rameau, T. Valla, T. E. Kidd, P. D. Johnson, Y. Hu, and Q. Li, *Europhys. Lett.* **81**, 57006 (2008).
- ¹⁰ Y. S. Hor, A. Richardella, P. Roushan, Y. Xia, J. G. Checkelsky, A. Yazdani, M. Z. Hasan, N. P. Ong, and R. J. Cava, *Phys. Rev. B* **79**, 195208 (2009).
- ¹¹ C. Chen, S. He, H. Weng, W. Zhang, L. Zhao, H. Liu, X. Jia, D. Mou, S. Liu, J. He, Y. Peng, Y. Feng, Z. Xie, G. Liu, X. Dong, J. Zhang, X. Wang, Q. Peng, Z. Wang, S. Zhang, F. Yang, C. Chen, Z. Xu, X. Dai, Z. Fang, and X. J. Zhou, *Proc. Natl. Acad. Sci. U. S. A.* **109**, 3694 (2012).
- ¹² M. T. Pettes, J. Maassen, I. Jo, M. S. Lundstrom, and L. Shi, *Nano Lett.* **13**, 5316 (2013).
- ¹³ B. M. Fregoso and S. Coh, *J. Phys.: Condens. Matter* **27**, 422001 (2015).
- ¹⁴ D. Hsieh, Y. Xia, D. Qian, L. Wray, J. H. Dil, F. Meier, J. Osterwalder, L. Patthey, J. G. Checkelsky, N. P. Ong, A. V. Fedorov, H. Lin, A. Bansil, D. Grauer, Y. S. Hor, R. J. Cava, and M. Z. Hasan, *Nature* **460**, 1101 (2009).
- ¹⁵ D. Kong, Y. Chen, J. J. Cha, Q. Zhang, J. G. Analytis, K. Lai, Z. Liu, S. S. Hong, K. J. Koski, S.-K. Mo, Z. Hussain, I. R. Fisher, Z.-X. Shen, and Y. Cui, *Nat. Nanotechnol.* **6**, 705 (2011).
- ¹⁶ J. Zhang, C.-Z. Chang, Z. Zhang, J. Wen, X. Feng, K. Li, M. Liu, K. He, L. Wang, X. Chen, Q.-K. Xue, X. Ma, and Y. Wang, *Nat. Commun.* **2**, 574 (2011).
- ¹⁷ D. Kim, S. Cho, N. P. Butch, P. Syers, K. Kirshenbaum, S. Adam, J. Paglione, and M. S. Fuhrer, *Nat. Phys.* **8**, 459 (2012).
- ¹⁸ W. Chen, S. Chen, D. C. Qi, X. Y. Gao, and A. T. S. Wee, *J. Am. Chem. Soc.* **129**, 10418 (2007).
- ¹⁹ C. Coletti, C. Riedl, D. S. Lee, B. Krauss, L. Patthey, K. von Klitzing, J. H. Smet, and U. Starke, *Phys. Rev. B* **81**, 235401 (2010).
- ²⁰ L. Yu, A. Zubair, E. J. G. Santos, X. Zhang, Y. Lin, Y. Zhang, and T. Palacios, *Nano Lett.* **15**, 4928 (2015).
- ²¹ J. Hwang, A. Wan, and A. Kahn, *Mater. Sci. Eng. R* **64**, 1 (2009).
- ²² D. Kong, W. Dang, J. J. Cha, H. Li, S. Meister, H. Peng, Z. Liu, and Y. Cui, *Nano Lett.* **10**, 2245 (2010).
- ²³ D. B. Williams and C. B. Carter, *Transmission Electron Microscopy: A Textbook for Materials Science* (Springer Science + Business Media, Inc., New York, 2009).
- ²⁴ Z. Ding, S. K. Bux, D. J. King, F. L. Chang, T.-H. Chen, S.-C. Huang, and R. B. Kaner, *J. Mater. Chem.* **19**, 2588 (2009).
- ²⁵ A. Mavrokefalos, M. T. Pettes, F. Zhou, and L. Shi, *Rev. Sci. Instrum.* **78**, 034901 (2007).
- ²⁶ H. J. Goldsmid, *Proc. Phys. Soc.* **71**, 633 (1958).
- ²⁷ J. P. Fleurial, L. Gaillard, R. Triboulet, H. Scherrer, and S. Scherrer, *J. Phys. Chem. Solids* **49**, 1237 (1988).
- ²⁸ K. Wang and C. Petrovic, *Phys. Rev. B* **86**, 155213 (2012).
- ²⁹ R. J. Mehta, Y. Zhang, C. Karthik, B. Singh, R. W. Siegel, T. Borca-Tasciuc, and G. Ramanath, *Nat. Mater.* **11**, 233 (2012).
- ³⁰ Y. Zhang, H. Wang, S. Krämer, Y. Shi, F. Zhang, M. Snedaker, K. Ding, M. Moskovits, G. J. Snyder, and G. D. Stucky, *ACS Nano* **5**, 3158 (2011).
- ³¹ C. Schumacher, K. G. Reinsberg, R. Rostek, L. Akinsinde, S. Baessler, S. Zastrow, G. Rampelberg, P. Woias, C. Detavernier, J. A. C. Broekaert, J. Bachmann, and K. Nielsch, *Adv. Energy Mater.* **3**, 95 (2013).
- ³² S. Nakajima, *J. Phys. Chem. Solids* **24**, 479 (1963).